

Concerted metabolic shift in early forebrain alters the CSF proteome and depends on cMYC downregulation for mitochondrial maturation

Ryann M Fame¹, Morgan L Shannon¹, Kevin F Chau^{1,2}, Joshua P Head¹, Maria K Lehtinen^{1,2*}

¹Department of Pathology, Boston Children's Hospital, Boston, Massachusetts, 02115, USA

²Program in Biological and Biomedical Sciences, Harvard Medical School, Boston, Massachusetts, 02115, USA

*Correspondence should be addressed to: maria.lehtinen@childrens.harvard.edu

Key Words: neurectoderm, neuroepithelium, metabolism, glycolysis, cMYC, mitochondria

SUMMARY STATEMENT

As neural progenitors mature from forebrain neuroectodermal cells to neuroepithelial cells, the mitochondrial landscape, metabolic components, and functional ability to employ glycolysis transition to favor oxidative phosphorylation.

ABSTRACT

Massive, coordinated cellular changes accompany the transition of central nervous system (CNS) progenitors from forebrain neuroectodermal cells to specified neuroepithelial cells. We previously found that c-MYC regulates the changing ribosomal and proteostatic landscapes in mouse forebrain precursors at embryonic days E8.5 vs. E10.5 (before vs. after neural tube closure; NTC) (Chau et al., 2018). Here we demonstrate parallel coordinated transcriptional changes in metabolic machinery during this same stage of forebrain specification. Progenitors showed striking mitochondrial structural changes transitioning from glycolytic cristae at E8.5, to more traditional mitochondria at E10.5. Accordingly, glucose usage shifted in progenitors such that E8.5 progenitors relied on glycolysis, and after NTC increasingly used oxidative phosphorylation. This metabolic shift was matched by changes in surrounding amniotic and cerebrospinal fluid proteomes. Importantly, these mitochondrial morphological shifts depend on c-MYC downregulation. Together, our findings demonstrate metabolic shifting accompanies dynamic organelle and proteostatic remodeling of progenitor cells during the earliest stages of forebrain development.

INTRODUCTION

Neural tube closure (neurulation) is a fundamental initial step of brain development. Prior to the massive cellular rearrangements involved in neural tube closure (Massarwa and Niswander, 2013), the neural plate comprises multipotent neural stem cells, including forebrain neurectodermal precursor cells. These neurectodermal precursors become progressively lineage restricted, first as neuroepithelial cells, then radial glial cells, and eventually give rise to all neurons and glia in the forebrain (Bjornsson et al., 2015). The initial steps of brain development associated with neurulation are accompanied by parallel and massive changes in the greater embryonic environment. Prior to neurulation, chorioallantoic branching and placental development have not been completed, contributing to a hypoxic external environment that is now known to be necessary for proper CNS development (Clough and Whittingham, 1983; Scully et al., 2016). Concurrently, the fluid that directly contacts the developing CNS changes from amniotic fluid (AF) to cerebrospinal fluid (CSF). These early brain fluids vary in composition and instructive capacities (Chau et al., 2015; Lehtinen et al., 2011). While advances in understanding the complex cellular, morphological and environmental processes surrounding neurulation have been made (Greene and Copp, 2014; Li et al., 2018; Massarwa and Niswander, 2013; Miyazawa et al., 2017; Wallingford et al., 2013; Wilde et al., 2014), still relatively little is known about the molecular processes instructing this foundational stage of brain formation.

The developmental time period surrounding neurulation is accompanied by changes in precursor cell transcriptomes, and in turn, organelle landscape (Chau et al., 2018). These changes include decreased c-MYC expression, mTOR pathway signaling, and ribosome biogenesis by E10.5 in mouse (Chau et al., 2018). In addition to these concerted changes, this developmental time involves increased vascularization and oxygenation of the brain (Vasudevan et al., 2008; Walls et al., 2008). Transcriptional analyses also show that genes

associated with mitochondrial function are enriched at E8.5 (Chau et al., 2018). Older studies using whole embryos identified changes in mitochondrial structure in cranial neural folds during the transition from gastrulation to neurulation. These changes include shifting from mitochondria with hallmarks of hypoxia, including swollen cristae and dense matrix (Morris and New, 1979), which are associated with glycolysis, to mitochondria with flattened cristae and lucid matrices more characteristic of high levels of oxidative phosphorylation. More recently, metabolomic analyses point to changes in metabolic intermediates and ATP content in the whole embryo and along the neural tube (Miyazawa et al., 2017; Miyazawa et al., 2018; Scully et al., 2016; Yamaguchi et al., 2017). Metabolic shifts can herald changes in cell fate, and missteps in metabolic pathways are implicated in a growing number of neurodevelopmental conditions (Fernandez et al., 2019; Salbaum and Kappen, 2010; Vallee and Vallee, 2018; Yamaguchi et al., 2017). Nevertheless, very little is known regarding the fundamental process of mitochondrial maturation and progenitor cell metabolism around the time of neural tube closure, when the mammalian forebrain first forms.

In light of these data, here we investigated metabolic changes during the early specification of the mammalian forebrain. Transmission electron microscopy (EM) and mitochondrial gene expression analyses revealed striking changes in mitochondrial morphology and activity. We then employed bioinformatics and molecular biology techniques to define a transcriptionally regulated metabolic transition in forebrain precursor cells from glycolysis at E8.5 to oxidative phosphorylation at E10.5. We probed intrinsic metabolic functional capability of E8.5 versus E10.5 and E12.5 neural progenitor cells and uncovered large-scale metabolic shifts in glucose metabolism indicating that the metabolism of E8.5 progenitors had the capacity to rely heavily on glycolysis, while E10.5 cells used more oxidative phosphorylation and E12.5 progenitors employed even more oxidative phosphorylation than either of the earlier stages. Finally, using transgenic mice to prolong c-

MYC expression in neural progenitors past its natural downregulation before E10.5, we found that the massive mitochondrial morphology shift is dependent on c-MYC downregulation. Taken together; these data demonstrate that the forebrain neurectoderm undergoes metabolic switching during this early, critical stage of forebrain specification.

RESULTS

Mitochondrial structural reorganization in the early forebrain

We previously observed major differences in transcriptional signatures of precursor cells from mouse forebrain at embryonic days E8.5 vs. E10.5 (before vs. after neural tube closure) including decreased c-MYC expression, mTOR pathway signaling, and ribosome biogenesis at E10.5 (Chau et al., 2018). These changes also suggested an accompanying shift in organelle landscape and nutrient sensing in E10.5 neuroepithelium (see Figure 2 in Chau et al., 2018). Prompted by these findings and together with previous reports of mitochondrial and metabolite changes in the whole embryo during the transition from gastrulation to neurulation (from ~E7-E9 (Miyazawa et al., 2017; Miyazawa et al., 2018), we investigated structural changes in mitochondria before and after neurulation. We performed transmission electron microscopy (EM) on neuroepithelial cells at E8.5 and E10.5 and characterized mitochondrial morphology (**Figure 1 A,B**) based on their classic features (Suldina et al., 2018). We observed a shift in mitochondrial morphology from predominantly displaying hallmarks of hypoxia, glycolysis and immaturity including condensed matrices with swollen cristae at E8.5, to more traditional mature mitochondria with lucid matrices and flat cristae at E10.5 (**Figure 1B**). We also observed a trend in differential mitochondrial associated membranes (MAMs) characterized by a shift toward fewer endoplasmic reticulum-mitochondrial contacts from E8.5 to E10.5 (**Figure 1A,C**). This finding is consistent with reports of metabolic changes associated with an excess cellular requirement for glucose and hypoxia-induced mitochondrial fragmentation (Rieusset, 2018; Wu et al., 2016).

In other systems, including in cancers that have altered oxygenation of tumor tissue, distinct mitochondrial morphologies are associated with either hypoxic environments (immature mitochondria) or normoxic environments (mature mitochondria) (Garcia-Prat et al., 2017; Gasparre et al., 2011; Suldina et al., 2018; Vander Heiden et al., 2009). Hif1- α is a

master regulator of oxygen homeostasis that, in other systems, controls angiogenesis, erythropoiesis, and glycolysis through transcriptional activation of target genes harboring an HRE (hypoxia response element) under hypoxic conditions (0.1-5.0% O₂). Accordingly, we observed increased Hif1- α protein expression at E8.5, but no change in either the transcript levels or hydroxylation status (**Figure 1 D,E**), suggesting that Hif1- α protein levels are stabilized at the translation or protein degradation levels, and not via differential transcription or post-translational modification. These elevated levels of Hif1- α protein are in agreement with previous reports that the early embryo prior to neural tube closure and choriallantoic branching is hypoxic (Dunwoodie, 2009; Miyazawa et al., 2017). The vascular system is also maturing during this developmental stage, as periventricular vessels first reach the dorsal telencephalon at E10.5 (Vasudevan et al., 2008; Walls et al., 2008). Consistent with these biological processes in the developing embryo, the E10.5 forebrain had increased levels of mitochondrial components associated with oxidative phosphorylation (e.g. Citrate Synthase, CS) as well as markers of non-hypoxic mitochondria (e.g. mitochondrial dynamism protein Mitofusin2 [Mfn2]) (**Figure 1F**). At the cellular level, each E8.5 neuroectodermal cell had fewer CS⁺ mitochondria than did the cells of the E10.5 neuroepithelium (**Figure 1 G,H**). Together, these data demonstrate widespread morphological and molecular changes in mitochondria of precursor cells during critical and early stages of forebrain development.

Decreased glycolytic machinery in E10.5 forebrain and CSF

Further investigation of changing metabolic components in forebrain precursors uncovered robust downregulation of the molecular machinery that governs glucose metabolism from E8.5 to E10.5. Glucose metabolism is a complex process, interconnected with multiple aspects of cellular function (**Figure 2A**, reviewed by Khacho and Slack, 2017,

2018). It can, therefore, be modulated at multiple levels beginning from the initial process of glucose uptake by glucose transporters (e.g. Glut1 and Glut3) to the presence of glycolytic, gluconeogenic, and oxidative phosphorylation machinery. Even if all the molecular machinery are present to perform oxidative phosphorylation and/or glycolysis, metabolism can quickly adapt to cellular needs with key switching components such as Ldh, Ucp2, Mtch1, and Atpif1, which alter the ratio of cellular materials that are shuttled through traditional oxidative phosphorylation vs. other pathways such as glycolysis and the pentose phosphate pathway (Cliff et al., 2017; Levine and Puzio-Kuter, 2010). Gene expression analysis from RNA sequencing data in E8.5 neurectoderm and E10.5 neuroepithelium (Chau et al., 2018) revealed that members of multiple metabolic pathways were enriched at E8.5 vs. E10.5 at the mRNA level, including general glucose usage, metabolic shifting, glycolysis, gluconeogenesis, and the pentose phosphate pathway (**Figure 2B, Figure S1A**). Key players in these processes were validated via qPCR including glycolytic enzymes *phosphoglycerate kinase 1 (pgk1)*; *lactate dehydrogenase a (ldha)*; and *aldolase a (aldoa)*, and the glucose transporters *slc2a1 (glut1)* and *slc1a3 (glut3)* (**Figure 2C, Figure S1B**). Protein levels reflected a similar trend in increased glucose uptake and glycolysis components at E8.5 evidenced by high levels of Glut1 and Ldha, while increased oxidative phosphorylation was suggested at E10.5 by increased expression of ATP Synthase/Complex V (**Figure 2D,E**). Together, these data demonstrate that forebrain precursor cells before and after neural tube closure house distinct metabolic machineries.

In addition to providing instructive signals for developing forebrain progenitors (Chau et al., 2015; Lehtinen et al., 2011), the early AF and CSF proteomes provide a biomarker signature of forebrain development by matching their fluid proteomes to the transcriptional changes of the forebrain, for example as was shown with changes associated with ribosome biogenesis (Chau et al., 2018). Consistent with these findings, nearly all metabolic proteins

detected and enriched in the E8.5 AF proteome (**Figures 3A,B**) matched the concurrent transcriptional changes in the E8.5 and E10.5 transcriptomes (**Figure 2B**). Not only were metabolic proteins less abundant in E10.5 CSF, but many were no longer detected therein (**Figures 3A,B**; (Chau et al., 2018; Chau et al., 2015)). The E8.5 AF vs. E10.5 AF were even more divergent (**Figure 3C,D**). Together, these data demonstrate that the changes in the AF and CSF proteomes during early forebrain development match the downregulation of metabolic machinery in the adjacent neuroepithelium (**Figures 3E,F**). Collectively, these data suggest that early forebrain precursors harness different metabolic pathways for ATP synthesis and production of anabolic intermediates to meet changing cellular energy and substrate demands.

Early forebrain undergoes metabolic switching to utilize less glycolysis after neural tube closure

Since metabolic processes can be regulated at multiple levels including transcription, translation, post-translational modification, and based on external cues such as substrate availability, we directly investigated whether the capacity for metabolic activity differs between E8.5 and E10.5 neuroepithelial cells. When glycolysis-derived lactate is exported from the cell, protons are also exported; therefore, extracellular acidification rates (ECAR) indicate glycolysis (**Figure 4A, Figure S1C**). Using the Agilent XF Seahorse technology, we simultaneously measured ECAR and mitochondrial oxygen consumption rate (OCR) to generate a live-cell bioenergetic profile. Unlike endpoint assays such as lactate, this test allowed us to detect changes in metabolic function in real time, providing a window on the earliest events of metabolic switching. The ECAR was then used to calculate glycolytic parameters in primary cultures of E8.5 and E10.5 forebrain neuroepithelium (**Figure 4A,**

Figure S1D). After microdissection of the E8.5 and E10.5 neuroepithelium, followed by dissociation and plating in glucose-free media (**Figure 4B**), we measured glucose utilization with the Seahorse XF Glycolysis Stress Test. This test is designed to measure the capacity of the glycolytic pathway in cell populations by driving them toward glycolysis and measuring their increase in glycolytic activity to meet bioenergetic demand (**Figure 4A**). The greater ECAR increase after glucose addition indicated that E8.5 neuroepithelial progenitors were more dependent on glucose than E10.5 neuroepithelial progenitors (**Figure 4C-E, Figure S1C-D**). After blocking mitochondrial ATP-synthase and, therefore, also the electron transport chain, with oligomycin, E8.5 progenitors still maintained higher ECAR, indicating larger capacity to buffer against compromised mitochondrial function via glycolysis usage, i.e. glycolytic capacity (**Figure 4C-E, Figure S1D**). The baseline OCR was higher in E8.5 progenitors than E10.5 progenitors, suggesting the possibility of an early intracellular energy source (**Figure S1C**), however both E8.5 and E10.5 progenitors showed a boost in the OCR after glucose addition and a decrease in OCR after oligomycin indicating that both cell types have functional mitochondria that employ oxidative phosphorylation (**Figure S1C**). It should be noted that, due to glycolytic rates and cellular availability, E8.5 and E10.5 cells were plated at different densities for comparison. Cellular density, even when normalized by cell number leads to somewhat different rates (**Figure S1D**). The results remain consistent with those presented, and as these data obtained from cultured cells show a snapshot in time, it may be that the native *in vivo* differences are even greater than these *in vitro* analyses are able to show.

To investigate the proportion of each cell type's acidification due to glycolysis, rather than other processes (including increased glutamate levels in excitatory neuron progenitors), we employed the Seahorse XF Glycolytic Rate Assay. This assay takes into account the ECAR, OCR, and buffer capacity of the media and uses a standard contribution rate of CO₂

to acidification that is determined experimentally in multiple cell lines and primary cell cultures including neural progenitors. Therefore, the Glycolytic Rate Assay allowed calculation of proton efflux rate (PER) in the presence of glucose followed by inhibition of the electron transport chain with rotenone and antimycin A (Rot/AA), which inhibits NADH ubiquinone reductase, and cytochrome c reductase, respectively. This was followed by inhibition of all glycolysis with the glucose analogue 2-deoxy-d-glucose (2-DG) (**Figure 4F**). We determined that the proportion of proton efflux due to glycolysis was highest in E8.5 progenitors, reduced in E10.5 progenitors, and was lowest in E12.5 progenitors (**Figure 4F, G**); the developmental stage when changes in mitochondrial function have been shown to induce the maturation factor NRF2 (Khacho et al., 2016; Khacho and Slack, 2017). Additionally, the proportion between mitochondrial oxygen consumption and glycolytic proton efflux drastically increased as the neuroepithelium matured from E8-E12.5 (**Figure 4H**). Taken together, these data functionally demonstrate that E8.5 forebrain precursors have more glycolytic capacity and are more dependent on extracellular glucose for their metabolism than E10.5 forebrain neuroepithelial progenitors. Conversely, E10.5 and E12.5 progenitors are more heavily reliant on mitochondrial oxidative phosphorylation processes for their metabolism. These data suggest key roles for glucose availability and regulation during this early, critical stage of forebrain development.

Downregulation of c-MYC is required for mitochondrial structural reorganization in neuroepithelial progenitors

Developmental downregulation of c-MYC is critical to controlling a shift in translation machinery and ribosome biogenesis during neural tube closure between E8.5 and E10.5 in mice (Chau et al., 2018). Because c-MYC targets are also involved in many

mitochondrial and hypoxia-related processes (Doe et al., 2012; Goetzman and Prochownik, 2018; Morrish and Hockenbery, 2014), we investigated mitochondria after experimentally extending the time and level of c-MYC expression in neuroepithelial progenitors by expressing a human c-MYC transgene in neuroepithelial progenitors by crossing *StopFLMYC* mice (Calado et al., 2012) with *Foxg1-Cre* (Hébert and McConnell, 2000). First, we performed transmission EM on neuroepithelial cells at E12.5 and characterized mitochondrial morphology (**Figure 5 A,B**, as in **Figure 1 A,B**) based on their classic features (Suldina et al., 2018). In contrast to traditional, more mature mitochondria with lucid matrices and thin cristae, E12.5 forebrain progenitors with prolonged c-MYC expression retained the striking mitochondrial morphology of immature, glycolytic, condensed matrices with swollen cristae (**Figure 5A,B**), approximating E8.5 forebrain precursors (**Figure 1A,B**). However, this morphological change was not reflected in MAMs (N=4 mice, % of mitochondria with EM contact \pm SEM: WT=20.2% \pm 0.8; MYC-OE= 21.9% \pm 1.6; p-value=0.63, t-test) or expression of canonical mitochondrial dynamics pathway-associated proteins such as OPA1 or PGC-1 α (**Figure S2C**). While MYC expression regulated a robust change in mitochondrial morphology, it was insufficient to drive a preference for glycolytic metabolism over oxidative phosphorylation as demonstrated by unchanged expression of glycolytic genes (**Figure 5C**, **Figure S2A**), although some genes in other metabolic pathways did change (**Figure 5D**, **Figure S2B**). Functionally, there was no change in the PER balance, OCR, or ECAR in progenitors under the conditions tested (**Figures 5E**, **Figure S2D**). This observation could potentially result from combinatorial effects due to c-MYC's potentially limited accessibility to chromatin following neurulation and/or the oxygenated/normoxic environment of the E12.5 embryo. Taken together, our findings support a model in which c-MYC expression in neuroepithelial progenitor cells regulates mitochondrial maturation in the early, developing forebrain.

DISCUSSION

Elucidating the metabolic contributions at the inception of the mammalian forebrain is paramount to understanding neural development. Our study reveals concerted changes in metabolic machinery during early specification of the mammalian forebrain. This work (1) uncovers striking changes in the mitochondrial landscape between neuroectodermal progenitors at E8.5 and neuroepithelial progenitors at E10.5; (2) shows that enhanced glycolysis and anabolic pathways serve as transcriptional signatures of early forebrain progenitor cells at E8.5; (3) reveals that the changing proteomes of the AF and CSF provide a biomarker signature that matches the concurrent, normal metabolic changes in the adjacent brain; (4) functionally demonstrates that E8.5 progenitors are more glycolytic than their E10.5 progeny; and (5) demonstrates prolonged c-MYC expression as sufficient to maintain mitochondria in a state with swollen cristae and condensed matrices, one part of the metabolic machinery present in proliferative, glycolytic, or hypoxic cells. We conclude that neural stem cells dynamically regulate their metabolism to meet their changing energy and anabolic needs.

Protein homeostasis and mitochondrial dynamics

Changes in organelle content and maturity are a common theme in fate specification. We previously demonstrated downregulation of ribosome biogenesis that corresponds with accompanying changes in protein synthesis in neural progenitors during the same timeframe that we investigate here (E8.5-E10.5; Chau et al., 2018). Additionally, tightly regulated proteostatic mechanisms are required for maintaining neural stem cell pluripotency (Garcia-Prat et al., 2017; Vilchez et al., 2012; Vilchez et al., 2014; You et al., 2015), and during human neuronal differentiation, widespread remodeling of translational machinery occurs via

differential mTOR signaling and differential translation of 3' UTRs (Blair et al., 2017). While the inputs to proteostasis are diverse and involve multiple organelles and molecular machines, the endoplasmic reticulum (ER) plays a key role in proteostasis via the ER unfolded protein response and through its roles regulating intracellular calcium (Garcia-Prat et al., 2017; Lee et al., 2017) and metabolism (Garcia-Prat et al., 2017). Both the ER unfolded protein response, and calcium regulation are achieved through coordination between the ER and the mitochondria. Here, we directly implicated mitochondria and metabolism as changing concurrently with linked protostatic shifts in the forebrain.

In later stages of corticogenesis, mitochondrial dynamics regulate stem cell fate decisions, mediated by reactive oxygen species (ROS) that directly stimulate NRF2 signaling, which suppresses self-renewal and promotes differentiation (Khacho et al., 2016; Khacho and Slack, 2017). Our new data fit into this context, showing that this process is not stagnate, but rather, is initiated prior to cortical progenitor specification, and continues into later stages of brain development and maturation. For example, cortical neuronal differentiation *in vitro* and postnatally *in vivo* results in changes in mitochondrial mass, increased oxidative phosphorylation and decreased glycolysis dependent on PI3K-Akt-mTOR signaling (Agostini et al., 2016); and in mature neurons, mitochondrial dynamics in presynaptic boutons are critical for maintaining neuronal health and avoiding excitatory neurotoxicity, via mitochondrial regulation of intracellular calcium clearance to control neurotransmitter release (Kwon et al., 2016). Thus, close coordination between proteostasis, intracellular calcium, and metabolism govern neural cell fate and long-term neuronal health. Our data bridge the gap between stem cell and cortical progenitor by demonstrating a transition in mitochondrial morphology and gene expression as the neuroectoderm develops and becomes more lineage-restricted neuroepithelium.

Hypoxia and neurodevelopmental metabolism

The overall embryonic environment changes dramatically from E8.5-E10.5, with the pre-neurulation embryo being hypoxic compared to the post-neurulation embryo (Clough and Whittingham, 1983; Scully et al., 2016). Studies have shown that this hypoxia is necessary for proper development of neural folds and neural crest (Morriss and New, 1979; Scully et al., 2016). Hypoxia can also alter mitochondrial dynamics by inducing mitochondrial fission and mitophagy, which is dependent on mitochondrial-ER interactions (Wu et al., 2016). More generally, in mature cells that normally rely on oxidative phosphorylation, hypoxia alone or in concert with gene expression changes can induce metabolic switching, which is associated with transferring metabolism to glycolysis and away from oxidative phosphorylation (Cliff et al., 2017; Goetzman and Prochownik, 2018; Morrish and Hockenbery, 2014). Recently, additional metabolic developmental studies in the context of neural tube closure have corroborated older studies (Morriss and New, 1979) showing that glucose metabolism along the neural tube is sensitive to extracellular oxygen levels (Miyazawa et al., 2018), and is also at least partially under the genetic control of *lin28a* (Miyazawa et al., 2017; Yamaguchi et al., 2017). Our original observation of changed organelle landscape (Chau et al., 2018), followed by unbiased transcriptome analyses performed in microdissected developing forebrain provide a “parts list” of metabolic machinery, which when paired with Seahorse data, demonstrate a functional shift in glucose utilization in the developing forebrain. Collectively, this active area of research is beginning to disentangle the extent to which early metabolism is flexible in response to specific external signals versus simply executing tightly regimented genetically programmed events.

In the disease setting, cancer cells usually remain glycolytic even in the presence of high oxygen concentration (sometimes termed “oxidative glycolysis”). Key to these findings, products of glycolysis itself, such as lactate, can induce a hypoxic response independent of

the canonical Hif1 α -dependent pathways using NDRG3 stabilization and Raf/Erk signaling (Lee et al., 2015). Thus, our data showing that the metabolic state of the developing forebrain is reflected in the associated AF/CSF raises the hypotheses that these surrounding fluids may provide biomarkers of normal developmental signatures or could even act as synchronizing feedback to the entire CNS about the metabolic state of the developing embryo.

Cellular metabolism adapts to changing anabolic and energetic demands of proliferation

From cancer research, it is known that transformed cells can alter their metabolism and mitochondrial morphology drastically to adapt to high proliferation rates and changing anabolic and energetic demands (Vander Heiden et al., 2009). Classically, Otto Warburg observed in 1924 that cancer cells metabolize glucose via glycolysis, in a manner that is distinct from that of cells in differentiated tissues (Warburg et al., 1927). Subsequent studies show that far from reflecting a mitochondrial defect, this metabolic switch is adaptive to proliferation by supporting the higher demand for equivalents of carbon and NADH than for ATP to provide the raw components needed for nucleotide and amino acid biosynthesis (Fantin et al., 2006; Vander Heiden et al., 2009). Pluripotent stem cells (induced and embryonic) also rely heavily on glycolysis (Cliff et al., 2017; Elstrom et al., 2004; Kondoh et al., 2007) and display similar mitochondrial morphologies to those that we observed in neurectoderm at E8.5 (Suldina et al., 2018). Comparing similarities between rapidly proliferating cancer cells and developmentally regulated proliferative progenitors reveals the common theme that cellular metabolism, through glycolysis, is adaptive for the demands of proliferative cells. Some caveats do exist from using the ECAR, PER, and, OCR readouts as a proxy for full metabolic analysis including the possibility of NADH contribution from the cytosol that results in O₂ consumption without equivalent acidification, CO₂ consumption

from carboxylation reactions, and lack of direct measurements of reactive species that may alter ECAR and OCR. However, the real-time readout enables an overview of progenitor metabolic capacity and glucose dependence. Here we demonstrate that the shift from glycolysis to oxidative phosphorylation is a tightly regulated transition between the E8.5 neuroectodermal progenitors vs. the more fate-restricted E10.5 neuroepithelial progenitors, and continues to be regulated as differentiation progresses to E12.5.

Metabolic shifts in differentiating stem cells correspond with MYC

c-MYC is well-known to be associated with regulating pathways necessary to maintain proliferative progenitors (Kerosuo and Bronner, 2016). While upstream controls, including nutrient sensing pathways (mTOR/PI3K, LKB1; Agostini et al., 2016; Buzzai et al., 2005; Hardie, 2007), have been shown to contribute to the glycolytic switching, c-MYC is also poised to be one of the master regulators of this process. Transcriptional targets of c-MYC include metabolite transporters and enzymes required for glucose metabolism, glutaminolysis, and biosynthesis, and inhibiting these downstream activities suppresses growth of c-MYC-driven tumors (Altman, et al 2016). Importantly, c-MYC targets include a large number of genes associated with mitochondrial morphology and function (Morrish and Hockenbery, 2014). In differentiating stem cells, MYC pathways are critical for developmental processes in the untransformed setting to maintain glycolysis in undifferentiated cells and as N-MYC and c-MYC are downregulated in endoderm and mesoderm, metabolic switching shifts more committed cells lineages to oxidative phosphorylation (Cliff et al., 2017; Goetzman and Prochownik, 2018). In fact, overexpression of N-myc in endoderm and mesodermal lineages is sufficient to re-induce glycolytic metabolism (Cliff et al., 2017). Strikingly, this metabolic switching does not occur as stem cells are allocated into the early ectodermal lineage (Cliff et al., 2017). Because c-MYC is

endogenously low in the E10.5 neuroepithelium, our MYC-OE data support the hypothesis that ectodermal lineages maintain high levels of glycolysis longer, and, rather, c-Myc downregulation and metabolic shifting occur later as the neuroectoderm commits to neuroepithelial lineage between E8.5 and E10.5.

While we report here that c-MYC must be downregulated for appropriate development of mitochondrial morphology in E12.5 neuroepithelium, the *ex-vivo* glycolysis assay and the RNA-Seq of *Nestin*-driven c-MYC overexpression system show that c-MYC may not be the sole regulator of glycolysis. These observations must be interpreted in the context of the development of the entire embryo, and it may be that c-MYC does not have access to its targets due to changes in chromatin landscape or other molecular checks and balances that are poorly understood that may prevent comprehensive evaluation of mechanisms at play via these assays. However, both hypoxia and c-MYC can stabilize Hif1 α and promote glycolysis and PI3K-AKT, which are also involved in glycolytic switching. In addition to influencing metabolism, c-MYC overexpression can induce over-proliferation phenotypes and tumors in brain epithelium (Shannon et al., 2018). While the pre-neurulation embryo is hypoxic compared to the post-neurulation embryo (Clough and Whittingham, 1983; Scully et al., 2016), glycolytic byproducts can also induce a hypoxic response independent of Hif1 α (Lee et al., 2015). Because the time period of c-MYC downregulation corresponds with the time period of shift from hypoxia to normoxia in the embryos, it is likely that while hypoxia itself can induce glycolytic responses, the concurrent high c-MYC levels act as an only partially redundant or reinforcing pathway to maintain the critical hypoxic and glycolytic state of these early progenitors (Cliff et al., 2017). In conclusion, while c-MYC itself stabilizes the hypoxic response in some systems (Doe et al., 2012; Goetzman and Prochownik, 2018), in the developing neuroepithelium, c-MYC is sufficient to

dramatically regulate mitochondrial morphology, but more than c-MYC alone is required to maintain glycolytic metabolism.

Implications for NTC and maternal glucose availability

The metabolic capacity of neural progenitors is of particular importance to the natural fluid environment of the developing brain. The *ex vivo* Seahorse analyses were performed in HEPES-buffered pH 7.4 minimal media to allow the calculations and to investigate the intrinsic potential of the progenitors. However, AF and CSF have buffering capacities that are distinct from each other and from the media. While the *in vivo* buffering capacity of CSF (pH 7.33) is better than that of blood due to high bicarbonate levels (Husted and Reed, 1977; Lee et al., 1969), early CSF is likely not buffered with bicarbonate, as the ChP, which expresses $\text{Cl}^-/\text{HCO}_3^-$ transporters, has not yet developed and matured (Liddelow et al., 2012). However, the embryonic CSF has a higher protein concentration than adult, which can provide additional buffering capacity. AF, on the other hand, has virtually no buffering capacity in chick at the analogous pre-neurulation stages in development (Randles and Romanoff, 1954). Taken together with our results, these data suggest that the acidic metabolic byproducts of glycolysis, particularly an early bolus of glucose, could severely alter the pH of the fluid environment of the developing brain. Such unbuffered acidosis can impact progenitor proliferation, survival, epigenetics, physiology, motility, and even metabolic reprogramming (White et al., 2017). All of these pH dependent effects in combination with intrinsic roles of altered metabolism might render the neurectoderm particularly sensitive to glucose availability.

Missteps in development increase vulnerability to neurologic disease. Our data open up a pathway for understanding how early forebrain metabolism critically contributes to more mature brain health. One relevant example is that of maternal diabetes, which has been shown

to be a risk factor for neural tube closure defects (Kucera, 1971; Martinez-Frias, 1994; Martinez-Frias et al., 1998). While glucose availability is not a usual limiting factor for glycolytic switching (Vander Heiden et al., 2009), high maternal glucose levels are associated with coordinated gene expression changes in the developing embryo (Pavlinkova et al., 2009; Salbaum and Kappen, 2010). Strikingly, the gene expression changes that result from high maternal blood glucose include enrichment of motifs for transcription factors that regulate response to oxidative stress or hypoxia in the E10.5 embryo (Salbaum and Kappen, 2010). These associations, coupled with our data supporting a massive change in glucose metabolism and potential for acidosis at times adjacent to neural tube closure, suggest a relationship between natural and diseased processes whereby metabolic misregulation increases vulnerability for neurodevelopmental disease and, therefore, indicate a potential window of intervention.

Taken together, our findings indicate large, coordinated changes in metabolic machinery in forebrain precursors during early brain development concurrent with neural tube closure, c-MYC downregulation, and the embryonic exit from hypoxia. Such a tight regulation of glycolytic metabolism at this time informs the relationship between neural precursor fate restriction and glucose usage, with the potential to guide future studies linking maternal metabolic dysregulation (maternal diabetes), and neural tube closure defects.

MATERIALS and METHODS

Key resources table

| Reagent type (species) or resource | Designation | Source or reference | Identifiers | Additional Information |
|---------------------------------------------------|--------------------------------------------------------------------------|-------------------------------------------------------------------------------------------------------------------|------------------|------------------------------------|
| strain, strain background (<i>Mus Musculus</i>) | CD-1 IGS Mouse (referred to as CD-1) | Charles River | Strain code: 022 | Wildtype timed pregnant mice |
| strain, strain background (<i>Mus Musculus</i>) | Foxg1 ^{tm1(cre)Skm} (referred as <i>Foxg1-cre</i>) | The Jackson Laboratory (Bar Harbor, ME) | MGI:5444670 | Maintained on a C57Bl/6 background |
| strain, strain background (<i>Mus Musculus</i>) | Gt(ROSA)26Sor ^{tm13(CAG-MYC, CD2*)Rsky} (referred as StopFLMYC) | The Jackson Laboratory | MGI:1932522 | Maintained on a C57Bl/6 background |
| antibody | Rabbit anti-Hif1 α | Cell Signaling | 3716S | 1:1000 |
| antibody | Rabbit anti-hydroxy Hif1 α (Pro564) | Cell Signaling | 3434S | 1:1000 |
| antibody | Rabbit anti-CS | Cell Signaling | 14309 | 1:1000 for WB; 1:50 for IHC |
| antibody | Rabbit anti-mitofusin2 | Cell Signaling | 9482S | 1:1000 |
| antibody | Rabbit anti-vinculin | Cell Signaling | 13901 | 1:1000 |
| antibody | Total OXPHOS Rodent WB Antibody Cocktail | Abcam | ab110413 | 1:250 |
| antibody | Mouse anti-Glut1 | Abcam | ab40084 | 1:1000 for WB; 1:100 for IHC |
| antibody | Rabbit anti-Ldha | Cell Signaling | 2012S | 1:1000 |
| RT-qPCR probe | Glut-1 (Slc2a1) | Applied Biosystems Taqman probe (FAM-MGB) | 4331182 | Mm00441480_m1 |
| RT-qPCR probe | Glut-3 (Slc2a3) | Applied Biosystems Taqman probe (FAM-MGB) | 4453320 | Mm00441483_m1 |
| RT-qPCR probe | Pgk1 | Applied Biosystems Taqman probe (FAM-MGB) | 4453320 | Mm00435617_m1 |
| RT-qPCR probe | Aldoa | Applied Biosystems Taqman probe (FAM-MGB) | 4448892 | Mm00833172_g1 |
| RT-qPCR probe | Ldha | Applied Biosystems Taqman probe (FAM-MGB) | 4448892 | Mm01612132_g1 |
| RT-qPCR probe | Hif1 α | Applied Biosystems Taqman probe (FAM-MGB) | 4453320 | Mm00468869_m1 |
| RT-qPCR probe | Eukaryotic 18S rRNA Endogenous Control | Applied Biosystems Taqman probe (VIC/MGB) | 4319413E | |
| commercial assay or kit | Glycolysis Stress Test | Agilent Seahorse | 103020-100 | Manufacturer's protocol |
| commercial assay or kit | Glycolysis Rate Assay | Agilent Seahorse | 103344-100 | Manufacturer's protocol |
| software, algorithm | DAVID | https://david.ncifcrf.gov/ | v6.7, 6.8 | RNAseq analysis |
| software, | GSEA | http://software.broadinstitute.org/gsea/index.jsp | v3.0 | RNAseq analysis |

| | | | | |
|---------------------|----------------|---------------------------------------------------|--------|----------------------|
| algorithm | | | | |
| software, algorithm | Prism | GraphPad | v7 | Statistical analysis |
| software, algorithm | Fiji (Image J) | https://fiji.sc/# | v2 | Image analysis |
| software, algorithm | Imaris | Bitplane | V7.7.1 | Image analysis |
| software, algorithm | Wave Desktop | Agilent | | Metabolic analysis |

Mice

Timed pregnant CD1 dams (*Mus musculus*) were obtained from Charles River Laboratories. StopFLMYC (Calado et al., 2012) mice (JAX: 020458) were maintained in a C57BL/6J genetic background and crossed with *Foxg1-cre* line (JAX: 004337) to generate MYC-OE mice, in which human *MYC* transgene is selectively expressed in neural progenitor cells. Due to phenotypes associated with *Foxg1-cre*^{+/-} mice (Hebert and McConnell, 2000), *Foxg1-cre*^{+/-}; StopFLMYC^{+/-} served as MYC-OE mice and *Foxg1-cre*^{+/-}; StopFLMYC^{+/+} were used as controls. All analyses were carried out using male and female mice. All animal experimentation was carried out under protocols approved by the IACUC of Boston Children's Hospital.

RNAseq data analysis

All analyses were performed using genes with FPKM > 1, which we considered as the threshold of expression, using previously published data (Chau et al., 2018). Functional annotation clustering was performed using DAVID v6.7 (<https://david.ncifcrf.gov/home.jsp>; (Huang et al., 2009). Gene set enrichment analysis was performed using GSEA v3 (Subramanian et al., 2005), gene sets were obtained from the Broad Institute Molecular Signatures Database (<http://software.broadinstitute.org/gsea/msigdb>).

Tissue processing

Samples were fixed in 4% paraformaldehyde (PFA). For cryosectioning, samples were incubated in the following series of solutions: 10% sucrose, 20% sucrose, 30% sucrose, 1:1 mixture of 30% sucrose and OCT (overnight), and OCT (1 hour). Samples were frozen in OCT.

Immunostaining

Cryosections were blocked and permeabilized (0.3% Triton-X-100 in PBS; 5% serum), incubated in primary antibodies overnight and secondary antibodies for 2 hours. Sections were counterstained with Hoechst 33342 (Invitrogen H3570, 1:10000) and mounted using Fluoromount-G (SouthernBiotech). The following primary antibodies were used: rabbit anti-CS (Cell Signaling 14309; 1:1000), mouse anti-Glut1 (Abcam ab40084; 1:1000). Secondary antibodies were selected from the Alexa series (Invitrogen, 1:500).

Immunoblotting

Tissues were homogenized in RIPA buffer supplemented with protease and phosphatase inhibitors. Protein concentration was determined by BCA assay (Thermo Scientific 23227). Samples were denatured in 2% SDS by heating at 37°C for 5 minutes. Equal amounts of proteins were loaded and separated by electrophoresis in a 4-15% gradient polyacrylamide gel (BioRad #1653320), transferred to a polyvinylidene difluoride (PVDF) membrane (250mA, 1.5 hours, on ice), blocked in filtered 5% BSA or milk in TBST, incubated with primary antibodies overnight at 4°C followed by HRP conjugated secondary antibodies (1:5000) for 1 hour, and visualized with ECL substrate. For hydroxylated protein analysis, the hydroxy-proteins were probed first, and then blots were stripped (Thermo Scientific 21059) and reprobed for total proteins. The following primary antibodies were used: rabbit anti-CS

(Cell Signaling 14309; 1:1000), mouse anti-Glut1 (Abcam ab40084; 1:1000), rabbit anti-Hif1 α (Cell Signaling 3716S; 1:1000), rabbit anti-hydroxy Hif1 α (Pro564) (Cell Signaling 3434S; 1:1000), rabbit anti-Mitofusin2 (Cell Signaling 9482S; 1:1000), rabbit anti-Vinculin (Cell Signaling 13901; 1:1000), rabbit anti-Ldha (Cell Signaling 2012S; 1:1000), mouse anti-PGC-1 α (4C1.3 EMD Millipore ST1202, 1:1000), mouse anti-OPA-1 (BD biosciences 612606, 1:1000), and Total OXPHOS Rodent WB Antibody Cocktail (Abcam ab110413; 1:250).

Transmission Electron Microscopy

All tissue processing, sectioning, and imaging was carried out at the Conventional Electron Microscopy Facility at Harvard Medical School. Forebrain tissues were fixed in 2.5% Glutaraldehyde/2% Paraformaldehyde in 0.1 M sodium cacodylate buffer (pH 7.4). They were then washed in 0.1M cacodylate buffer and postfixed with 1% Osmiumtetroxide (OsO₄)/1.5% Potassiumferrocyanide (KFeCN₆) for one hour, washed in water three times and incubated in 1% aqueous uranyl acetate for one hour. This was followed by two washes in water and subsequent dehydration in grades of alcohol (10 minutes each; 50%, 70%, 90%, 2x10min 100%). Samples were then incubated in propyleneoxide for one hour and infiltrated overnight in a 1:1 mixture of propyleneoxide and TAAB Epon (Marivac Canada Inc. St. Laurent, Canada). The following day, the samples were embedded in TAAB Epon and polymerized at 60 degrees C for 48 hours. Ultrathin sections (about 80nm) were cut on a Reichert Ultracut-S microtome, and picked up onto copper grids stained with lead citrate. Sections were examined in a JEOL 1200EX Transmission electron microscope or a TecnaiG² Spirit BioTWIN. Images were recorded with an AMT 2k CCD camera.

Mitochondrial quantification was performed by hand using the parameters outlined in (Suldina, et al. 2018) by an author blinded to all conditions (age, embryo). Any mitochondria

with unclear or out-of-plane cristae, were labeled “blurry” and excluded. For each condition, analyses were performed across multiple individual embryos (N=3 for each age; N=4 for each genetic condition in MYC-OE experiments). From each embryo, 15-20 fields of view were imaged at 10,000x and each mitochondrion was analyzed individually for morphology metrics. Each different field of view represented a unique cell or cells, and fields of view were chosen within the most apical layer of cells. The analyses between E8.5 and E10.5 included a total of 946 mitochondria; the analysis of control and MYC-OE included a total of 2,196 mitochondria.

Mitochondrial Quantification

Mitochondrial quantification was performed using Imaris (Bitplane). For 1 image per individual (N=3 at each age), CS⁺ mitochondrial number was calculated within a 63x field of view. The region of interest was created by hand tracing a 3-D surface containing only mesenchyme, only neuroectoderm, or only neuroepithelium, depending on the age. Mitochondria were then counted by the Imaris software using the “spots” tool, with estimated XY diameter of 0.8µm and an estimated Z diameter of 1.99 µm and with automatic background subtraction “on”, and quality above the automatic threshold. Nuclei were counted using the “spots” tool, with estimated XY diameter of 3.5 µm and an estimated Z diameter of 4.5 µm and with automatic background subtraction “on”, and quality above the automatic threshold. The number of mitochondria per cell was calculated by dividing the total number of mitochondria by the total number of nuclei.

Forebrain epithelium cell isolation

Forebrain epithelium at E8.5, E10.5, and E12.5 was dissected as described (Chau et al., 2015). Each sample comprised forebrain epithelial tissues pooled across one litter. Briefly,

embryos were removed from the uteri in HBSS and forebrain tissues were collected and digested in 2.5% pancreatin/0.25% trypsin for 30 min (E8.5), 40 min (E10.5) or 20 min (E12.5). The digest was stopped with 10% horse serum and 0.01% DNase in HBSS. Neuroectodermal/ neuroepithelial cells were separated from adjacent tissue using tungsten needles and dissociated in 1% Trypsin, 0.01% DNase in Ca^{2+} /Mg-free HBSS. Cells were washed in 10% FBS, 0.01% DNase in 1x DMEM, counted, then transferred to Seahorse XF Base Medium (Agilent, 102353-100) supplemented with 1mM L-glutamine at pH 7.4

Quantitative RT-PCR

For mRNA expression analyses, whole brains at E8.5 and E10.5 were dissected and pooled across one litter for each N. RNA was isolated using the RecoverAll Total Nucleic Acid Isolation Kit (Ambion) following manufacturer's specifications. Extracted RNA was quantified spectrophotometrically and 100ng was reverse-transcribed into cDNA using the ImProm-II Reverse Transcription System (Promega) following manufacturer's specifications. RT-qPCRs were performed in duplicate using Taqman Gene Expression Assays and Taqman Gene Expression Master Mix (Applied Biosystems) with eukaryotic *18s* as an internal control. Cycling was executed using the StepOnePlus Real-Time PCR System (Invitrogen) and analysis of relative gene expression was performed using the $2^{-\Delta\Delta\text{CT}}$ method (Livak and Schmittgen, 2001). Technical replicates were averaged for their cycling thresholds and further calculations were performed with those means.

Seahorse Metabolic Analysis

E8.5, E10.5, and E12.5 cells were plated on Seahorse XFe96 cell culture microplates (Agilent, 101085-004) coated with Cell TAK (Corning), in Seahorse XF Base Medium

(Agilent, 102353-100) supplemented with 1mM L-glutamine and 1mM pyruvate at pH7.4, centrifuged at 500rcf for 1 minute without break, and incubated for 1 hour at 37 °C in a non-CO₂ incubator. Extracellular acidification rates (ECAR) and oxygen consumption rates (OCR) were measured via the glycolytic stress test assay (Agilent, 103020-100) with a Seahorse XFe96Analyzer (Agilent) following the manufacturer's protocols. Data were processed using Wave software (Agilent) and standardized to cell number. The glycolytic rate measurements were calculated as the difference in ECAR measurements before and after glucose injection and glycolytic capacity measurements were calculated as the ECAR measurements following oligomycin treatment subtracted from the initial baseline measurements, as described by the manufacturer's protocol (Agilent, 103020-100). OCR rates were calculated as the difference in OCR measurements following glucose injection and the OCR measurements after oligomycin injection. The combined analysis includes 3 distinct experiments. The individual analyses were performed with pooled litters at each age and distributed into 6-12 wells depending on cell availability. Because of the detection limits of the system and the vastly different metabolic signatures, E8.5 progenitors were plated at 25,000 cells per well and E10.5 and E12.5 progenitors were plated at 50,000 cells per well. Data were normalized by cell number (per 1,000 cells). The low levels of E10.5 glycolysis precluded extensive analysis of 25,000 cells/ well and the low yield from E8.5 progenitors precluded sufficient technical replicates at 50,000 cells/well. However, cellular density, even when normalized by cell number leads to different rates (**Figure S1**). While the results remain consistent with those presented, it may be that the native *in vivo* differences are likely even greater than these *in vitro* analyses are able to show.

For proton efflux rate (PER) calculations, E10.5, and E12.5 cells were plated at 50,000 cells per well and E8.5 cells were plated at 25,000 cells per well on Seahorse XFe96 cell culture microplates (Agilent, 101085-004) coated with Cell TAK (Corning), in Seahorse

XF Base Medium pH=7.4 (Agilent, 102353-100) supplemented with 2mM L-glutamine, 0.18% glucose, and 1mM pyruvate, centrifuged at 500rcf for 1 minute without break, and incubated for 1 hour at 37 °C in a non-CO₂ incubator. PER was measured via the glycolytic rate assay (Agilent, 103344-100) using a Seahorse XFe96Analyzer (Agilent) following the manufacturer's protocols. Data were processed using Wave software (Agilent) using the CO₂ contribution factor (CCF) of 0.61 as calculated for XFe96 by Agilent for over 20 cell lines including neuronal progenitors, and standardized to cell number (per 1,000 cells). When only one experiment is represented, each data point represents the average of multiple wells for one condition (with error bars representing SE), when multiple experiments are represented; each data point is the average of an entire experiment.

Statistical Analysis

Biological replicates (N) were defined as samples from distinct individuals, analyzed either in the same experiment or within multiple experiments. Some samples were pooled across multiple litters so as to reduce inter-litter variability. Samples were allocated into groups based solely on the gestational age without respect to sex (both males and females were included). Statistical analyses were performed using Prism 7 or R. Outliers were excluded using ROUT method (Q= 1%). Appropriate statistical tests were selected based on the distribution of data, homogeneity of variances, and sample size. F tests or Bartlett's tests were used to assess homogeneity of variances between data sets. Parametric tests (T test, ANOVA) were used only if data were normally distributed and variances were approximately equal. Otherwise, nonparametric alternatives were chosen. Data are presented as means \pm standard deviation (SD). If multiple measurements were taken from a single individual, data are presented as means \pm standard errors of the mean (SEMs). Please refer to figure legends

for statistical tests used and sample size. P values < 0.05 were considered significant (*P≤0.05, **P≤0.01, ***P≤0.001, ****P≤0.0001).

ACKNOWLEDGEMENTS

We thank members of the Lehtinen and Fleming labs for helpful discussions and M. Ericsson for experimental advice and assistance.

FUNDING

We are grateful for the following support: NIH T32 HL110852 (RMF and KFC), NSF Graduate Research Fellowship (KFC), NIH R01 NS088566 (MKL), BCH IDDRC 1U54HD090255, and the New York Stem Cell Foundation. M.K. Lehtinen is a New York Stem Cell Foundation – Robertson Investigator.

COMPETING INTERESTS

The authors declare that no competing interests exist.

REFERENCES

- Agostini, M., Romeo, F., Inoue, S., Niklison-Chirou, M.V., Elia, A.J., Dinsdale, D., Morone, N., Knight, R.A., Mak, T.W., and Melino, G. (2016). Metabolic reprogramming during neuronal differentiation. *Cell Death Differ* 23, 1502-1514.
- Bjornsson, C.S., Apostolopoulou, M., Tian, Y., and Temple, S. (2015). It takes a village: constructing the neurogenic niche. *Dev Cell* 32, 435-446.
- Blair, J.D., Hockemeyer, D., Doudna, J.A., Bateup, H.S., and Floor, S.N. (2017). Widespread Translational Remodeling during Human Neuronal Differentiation. *Cell Rep* 21, 2005-2016.
- Buzzai, M., Bauer, D.E., Jones, R.G., Deberardinis, R.J., Hatzivassiliou, G., Elstrom, R.L., and Thompson, C.B. (2005). The glucose dependence of Akt-transformed cells can be reversed by pharmacologic activation of fatty acid beta-oxidation. *Oncogene* 24, 4165-4173.
- Calado, D.P., Sasaki, Y., Godinho, S.A., Pellerin, A., Kochert, K., Sleckman, B.P., de Alboran, I.M., Janz, M., Rodig, S., and Rajewsky, K. (2012). The cell-cycle regulator c-Myc is essential for the formation and maintenance of germinal centers. *Nature immunology* 13, 1092-1100.
- Chau, K.F., Shannon, M.L., Fame, R.M., Fonseca, E., Mullan, H., Johnson, M.B., Sendamarai, A.K., Springel, M.W., Laurent, B., and Lehtinen, M.K. (2018). Downregulation of ribosome biogenesis during early forebrain development. *eLife* 7.
- Chau, K.F., Springel, M.W., Broadbelt, K.G., Park, H.Y., Topal, S., Lun, M.P., Mullan, H., Maynard, T., Steen, H., LaMantia, A.S., *et al.* (2015). Progressive Differentiation and Instructive Capacities of Amniotic Fluid and Cerebrospinal Fluid Proteomes following Neural Tube Closure. *Dev Cell* 35, 789-802.
- Cliff, T.S., Wu, T., Boward, B.R., Yin, A., Yin, H., Glushka, J.N., Prestegard, J.H., and Dalton, S. (2017). MYC Controls Human Pluripotent Stem Cell Fate Decisions through Regulation of Metabolic Flux. *Cell stem cell* 21, 502-516 e509.
- Clough, J.R., and Whittingham, D.G. (1983). Metabolism of [14C]glucose by postimplantation mouse embryos in vitro. *Journal of embryology and experimental morphology* 74, 133-142.
- Doe, M.R., Ascano, J.M., Kaur, M., and Cole, M.D. (2012). Myc posttranscriptionally induces HIF1 protein and target gene expression in normal and cancer cells. *Cancer Res* 72, 949-957.
- Dunwoodie, S.L. (2009). The role of hypoxia in development of the Mammalian embryo. *Dev Cell* 17, 755-773.

Elstrom, R.L., Bauer, D.E., Buzzai, M., Karnauskas, R., Harris, M.H., Plas, D.R., Zhuang, H., Cinalli, R.M., Alavi, A., Rudin, C.M., *et al.* (2004). Akt stimulates aerobic glycolysis in cancer cells. *Cancer Res* 64, 3892-3899.

Fantin, V.R., St-Pierre, J., and Leder, P. (2006). Attenuation of LDH-A expression uncovers a link between glycolysis, mitochondrial physiology, and tumor maintenance. *Cancer cell* 9, 425-434.

Fernandez, A., Meechan, D.W., Karpinski, B.A., Paronett, E.M., Bryan, C.A., Rutz, H.L., Radin, E.A., Lubin, N., Bonner, E.R., Popratiloff, A., *et al.* (2019). Mitochondrial Dysfunction Leads to Cortical Under-Connectivity and Cognitive Impairment. *Neuron* 102, 1127-1142 e1123.

Garcia-Prat, L., Sousa-Victor, P., and Munoz-Canoves, P. (2017). Proteostatic and Metabolic Control of Stemness. *Cell stem cell* 20, 593-608.

Gasparre, G., Romeo, G., Rugolo, M., and Porcelli, A.M. (2011). Learning from oncocytic tumors: Why choose inefficient mitochondria? *Biochim Biophys Acta* 1807, 633-642.

Goetzman, E.S., and Prochownik, E.V. (2018). The Role for Myc in Coordinating Glycolysis, Oxidative Phosphorylation, Glutaminolysis, and Fatty Acid Metabolism in Normal and Neoplastic Tissues. *Frontiers in endocrinology* 9, 129.

Greene, N.D., and Copp, A.J. (2014). Neural tube defects. *Annu Rev Neurosci* 37, 221-242.

Hardie, D.G. (2007). AMP-activated/SNF1 protein kinases: conserved guardians of cellular energy. *Nat Rev Mol Cell Biol* 8, 774-785.

Hebert, J.M., and McConnell, S.K. (2000). Targeting of cre to the Foxg1 (BF-1) locus mediates loxP recombination in the telencephalon and other developing head structures. *Dev Biol* 222, 296-306.

Huang, D.W.a.W., Sherman, B.T., and Lempicki, R.A. (2009). Systematic and integrative analysis of large gene lists using DAVID bioinformatics resources. *Nature protocols* 4, 44-57.

Husted, R.F., and Reed, D.J. (1977). Regulation of cerebrospinal fluid bicarbonate by the cat choroid plexus. *The Journal of physiology* 267, 411-428.

Kerosuo, L., and Bronner, M.E. (2016). cMyc Regulates the Size of the Premigratory Neural Crest Stem Cell Pool. *Cell Rep* 17, 2648-2659.

Khacho, M., Clark, A., Svoboda, D.S., Azzi, J., MacLaurin, J.G., Meghaizel, C., Sesaki, H., Lagace, D.C., Germain, M., Harper, M.E., *et al.* (2016). Mitochondrial Dynamics Impacts Stem Cell Identity and Fate Decisions by Regulating a Nuclear Transcriptional Program. *Cell stem cell* 19, 232-247.

Khacho, M., and Slack, R.S. (2017). Mitochondrial activity in the regulation of stem cell self-renewal and differentiation. *Current opinion in cell biology* 49, 1-8.

Khacho, M., and Slack, R.S. (2018). Mitochondrial dynamics in the regulation of neurogenesis: From development to the adult brain. *Dev Dyn* 247, 47-53.

Kondoh, H., Lleonart, M.E., Nakashima, Y., Yokode, M., Tanaka, M., Bernard, D., Gil, J., and Beach, D. (2007). A high glycolytic flux supports the proliferative potential of murine embryonic stem cells. *Antioxidants & redox signaling* 9, 293-299.

Kucera, J. (1971). Rate and type of congenital anomalies among offspring of diabetic women. *The Journal of reproductive medicine* 7, 73-82.

Kwon, S.K., Sando, R., 3rd, Lewis, T.L., Hirabayashi, Y., Maximov, A., and Polleux, F. (2016). LKB1 Regulates Mitochondria-Dependent Presynaptic Calcium Clearance and Neurotransmitter Release Properties at Excitatory Synapses along Cortical Axons. *PLoS biology* 14, e1002516.

Lee, D.C., Sohn, H.A., Park, Z.Y., Oh, S., Kang, Y.K., Lee, K.M., Kang, M., Jang, Y.J., Yang, S.J., Hong, Y.K., *et al.* (2015). A lactate-induced response to hypoxia. *Cell* 161, 595-609.

Lee, H.J., Gutierrez-Garcia, R., and Vilchez, D. (2017). Embryonic stem cells: a novel paradigm to study proteostasis? *The FEBS journal* 284, 391-398.

Lee, J.E., Chu, F., Posner, J.B., and Plum, F. (1969). Buffering capacity of cerebrospinal fluid in acute respiratory acidosis in dogs. *The American journal of physiology* 217, 1035-1038.

Lehtinen, M.K., Zappaterra, M.W., Chen, X., Yang, Y.J., Hill, A.D., Lun, M., Maynard, T., Gonzalez, D., Kim, S., Ye, P., *et al.* (2011). The cerebrospinal fluid provides a proliferative niche for neural progenitor cells. *Neuron* 69, 893-905.

Levine, A.J., and Puzio-Kuter, A.M. (2010). The control of the metabolic switch in cancers by oncogenes and tumor suppressor genes. *Science* 330, 1340-1344.

Li, H., Zhang, J., and Niswander, L. (2018). Zinc deficiency causes neural tube defects through attenuation of p53 ubiquitylation. *Development* 145.

Liddelow, S.A., Temple, S., Mollgard, K., Gehwolf, R., Wagner, A., Bauer, H., Bauer, H.C., Phoenix, T.N., Dziegielewska, K.M., and Saunders, N.R. (2012). Molecular characterisation of transport mechanisms at the developing mouse blood-CSF interface: a transcriptome approach. *PLoS One* 7, e33554.

Livak, K.J., and Schmittgen, T.D. (2001). Analysis of relative gene expression data using real-time quantitative PCR and the 2(-Delta Delta C(T)) Method. *Methods* 25, 402-408.

Martinez-Frias, M.L. (1994). Epidemiological analysis of outcomes of pregnancy in diabetic mothers: identification of the most characteristic and most frequent congenital anomalies. *Am J Med Genet* 51, 108-113.

Martinez-Frias, M.L., Bermejo, E., Rodriguez-Pinilla, E., Prieto, L., and Frias, J.L. (1998). Epidemiological analysis of outcomes of pregnancy in gestational diabetic mothers. *Am J Med Genet* 78, 140-145.

Massarwa, R., and Niswander, L. (2013). In toto live imaging of mouse morphogenesis and new insights into neural tube closure. *Development* 140, 226-236.

Miyazawa, H., Yamaguchi, Y., Sugiura, Y., Honda, K., Kondo, K., Matsuda, F., Yamamoto, T., Suematsu, M., and Miura, M. (2017). Rewiring of embryonic glucose metabolism via suppression of PFK-1 and aldolase during mouse chorioallantoic branching. *Development* 144, 63-73.

Miyazawa, H., Yamamoto, M., Yamaguchi, Y., and Miura, M. (2018). Mammalian embryos show metabolic plasticity toward the surrounding environment during neural tube closure. *Genes Cells* 23, 794-802.

Morrish, F., and Hockenbery, D. (2014). MYC and mitochondrial biogenesis. *Cold Spring Harbor perspectives in medicine* 4.

Morriss, G.M., and New, D.A. (1979). Effect of oxygen concentration on morphogenesis of cranial neural folds and neural crest in cultured rat embryos. *Journal of embryology and experimental morphology* 54, 17-35.

Pavlinkova, G., Salbaum, J.M., and Kappen, C. (2009). Maternal diabetes alters transcriptional programs in the developing embryo. *BMC Genomics* 10, 274.

Randles, C.A., Jr., and Romanoff, A.L. (1954). The buffering capacities of allantoic and amniotic fluids of the chick. *Arch Biochem Biophys* 49, 160-167.

Rieusset, J. (2018). The role of endoplasmic reticulum-mitochondria contact sites in the control of glucose homeostasis: an update. *Cell death & disease* 9, 388.

- Salbaum, J.M., and Kappen, C. (2010). Neural tube defect genes and maternal diabetes during pregnancy. *Birth defects research Part A, Clinical and molecular teratology* 88, 601-611.
- Scully, D., Keane, E., Batt, E., Karunakaran, P., Higgins, D.F., and Itasaki, N. (2016). Hypoxia promotes production of neural crest cells in the embryonic head. *Development* 143, 1742-1752.
- Shannon, M.L., Fame, R.M., Chau, K.F., Dani, N., Calicchio, M.L., Geleoc, G.S., Lidov, H.G.W., Alexandrescu, S., and Lehtinen, M.K. (2018). Mice Expressing Myc in Neural Precursors Develop Choroid Plexus and Ciliary Body Tumors. *The American journal of pathology* 188, 1334-1344.
- Subramanian, A., Tamayo, P., Mootha, V.K., Mukherjee, S., Ebert, B.L., Gillette, M.A., Paulovich, A., Pomeroy, S.L., Golub, T.R., Lander, E.S., *et al.* (2005). Gene set enrichment analysis: A knowledge-based approach for interpreting genome-wide expression profiles. *Proceedings of the National Academy of Sciences of the United States of America* 102, 15545-15550.
- Suldina, L.A., Morozova, K.N., Menzorov, A.G., Kizilova, E.A., and Kiseleva, E. (2018). Mitochondria structural reorganization during mouse embryonic stem cell derivation. *Protoplasma* 255, 1373-1386.
- Vallee, A., and Vallee, J.N. (2018). Warburg effect hypothesis in autism Spectrum disorders. *Molecular brain* 11, 1.
- Vander Heiden, M.G., Cantley, L.C., and Thompson, C.B. (2009). Understanding the Warburg effect: the metabolic requirements of cell proliferation. *Science* 324, 1029-1033.
- Vasudevan, A., Long, J.E., Crandall, J.E., Rubenstein, J.L., and Bhide, P.G. (2008). Compartment-specific transcription factors orchestrate angiogenesis gradients in the embryonic brain. *Nat Neurosci* 11, 429-439.
- Vilchez, D., Boyer, L., Morante, I., Lutz, M., Merkwirth, C., Joyce, D., Spencer, B., Page, L., Masliah, E., Berggren, W.T., *et al.* (2012). Increased proteasome activity in human embryonic stem cells is regulated by PSMD11. *Nature* 489, 304-308.
- Vilchez, D., Simic, M.S., and Dillin, A. (2014). Proteostasis and aging of stem cells. *Trends in cell biology* 24, 161-170.
- Wallingford, J.B., Niswander, L.A., Shaw, G.M., and Finnell, R.H. (2013). The continuing challenge of understanding, preventing, and treating neural tube defects. *Science* 339, 1222002.
- Walls, J.R., Coultas, L., Rossant, J., and Henkelman, R.M. (2008). Three-dimensional analysis of vascular development in the mouse embryo. *PLoS One* 3, e2853.

Warburg, O., Wind, F., and Negelein, E. (1927). The Metabolism of Tumors in the Body. *The Journal of general physiology* 8, 519-530.

White, K.A., Grillo-Hill, B.K., and Barber, D.L. (2017). Cancer cell behaviors mediated by dysregulated pH dynamics at a glance. *J Cell Sci* 130, 663-669.

Wilde, J.J., Petersen, J.R., and Niswander, L. (2014). Genetic, epigenetic, and environmental contributions to neural tube closure. *Annual review of genetics* 48, 583-611.

Wu, W., Lin, C., Wu, K., Jiang, L., Wang, X., Li, W., Zhuang, H., Zhang, X., Chen, H., Li, S., *et al.* (2016). FUNDC1 regulates mitochondrial dynamics at the ER-mitochondrial contact site under hypoxic conditions. *EMBO J* 35, 1368-1384.

Yamaguchi, Y., Miyazawa, H., and Miura, M. (2017). Neural tube closure and embryonic metabolism. *Congenital anomalies* 57, 134-137.

You, K.T., Park, J., and Kim, V.N. (2015). Role of the small subunit processome in the maintenance of pluripotent stem cells. *Genes Dev* 29, 2004-2009.

Figures

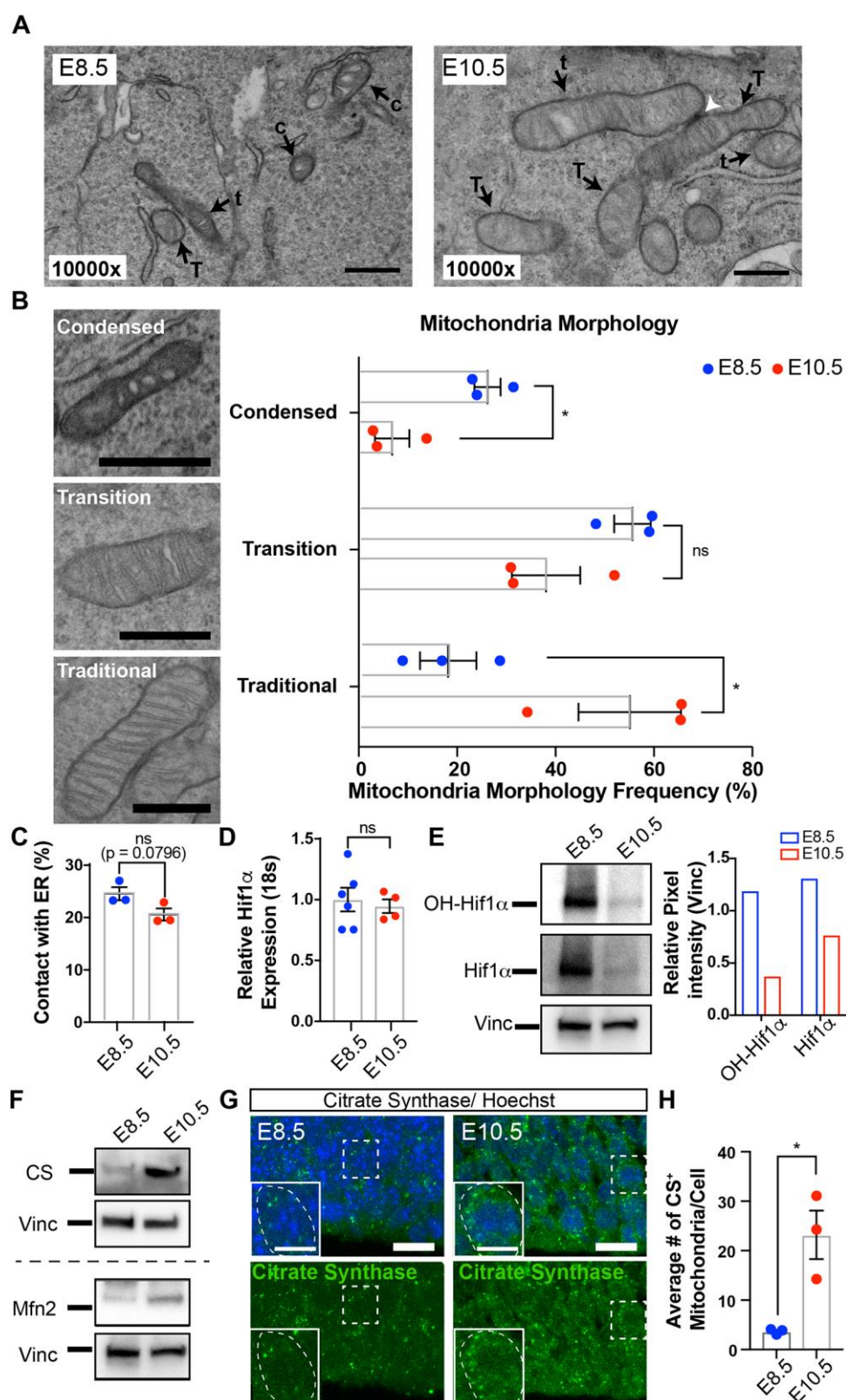


Figure 1. Mitochondrial structural reorganization and molecular maturation in the early forebrain neuroepithelium. (A) Mitochondrial morphology shifted in neuroepithelial

cells from E8.5 to E10.5. Arrows (black): mitochondria (annotated as T: traditional, t: transition, and c: condensed). Arrowhead (white): intermitochondrial junction. **(B)** Mitochondria at E8.5 were more likely to have condensed mitochondria with dense matrix and swollen cristae, while mitochondria in E10.5 neuroepithelial cells were more traditional with lucid matrices and thin cristae; t-test: *, $p < 0.05$; ns, non-significant $p = 0.0896$, error bars = SEM. **(C)** We observed a trend that approached significance in endoplasmic reticulum-mitochondrial contacts between these two ages; t-test: ns, non-significant $p = 0.0796$, error bars = SEM. **(D)** Expression of Hif1- α mRNA by qPCR was not changed between E8.5 neur ectoderm and E10.5 neuroepithelium. Data are expressed as relative to eukaryotic *18s*; t-test: ns, non-significant $p = 0.6418$, error bars = SD. **(E)** Hif1- α protein, however, was preferentially stabilized at E8.5, although transcription was unchanged. **(F)** In the forebrain, there was more overall CS protein and mitochondria showed more potential for dynamism, as evidenced by higher Mitofusin2 (Mfn2) expression. **(G,H)** At E10.5, mitochondria were more mature with high expression of the critical citric acid cycle component citrate synthase (CS) per cell (dashed box is area of inset, dashed white line outlines the cell in the inset); t-test: *, $p < 0.05$, error bars = SEM. Scale bar: (A) 500nm; (C) 10 μ m, inset 5 μ m.

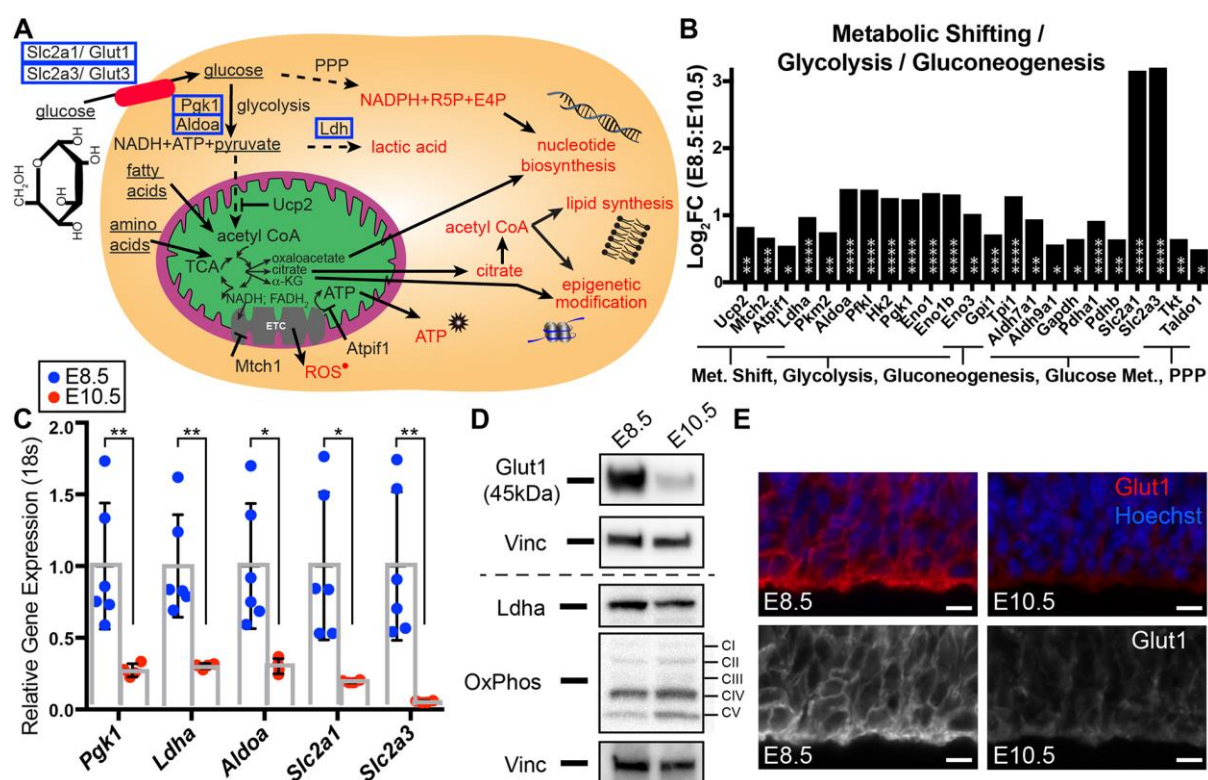


Figure 2. Gene and protein expression suggest metabolic switch away from glycolysis during E8.5 to E10.5 transition. (A) The cell can use glucose for multiple processes including glycolysis, oxidative phosphorylation, and nucleotide biosynthesis through the pentose phosphate pathway (PPP). Key metabolic switching factors (Ldh, Ucp2, Mth1, Atp1f1) shift the metabolic state between primarily glycolytic and primarily oxidative phosphorylation. Blue boxes indicate individual candidates selected for further validation. (B) Molecular components of metabolic shifting, glycolysis, gluconeogenesis, glucose metabolism, and PPP were enriched in the E8.5 neuroepithelium (N=2 biological replicates, each a pooled litter) with respect to the E10.5 neuroepithelium (N=2 biological replicates, each a pooled litter) (log₂fold change >0) cuffdiff v2 with q value: *, q < 0.1; **, q < 0.001; ***, q < 0.0001; ****, q < 0.00001; see Chau, et al 2018. (C) Individual components of these pathways (*pgk1*, *ldha*, *aldoa*, *slc2a1* (glut1), and *slc2a3* (glut3)) were validated by qPCR to be

downregulated in E10.5 neuroepithelium. Data are expressed as relative to eukaryotic *18s*. t-test: *, $p < 0.05$; **, $p < 0.01$, error bars = SEM. **(D-E)** This transcriptional enrichment was also reflected in protein levels. Scale bar (E) 10 μm .

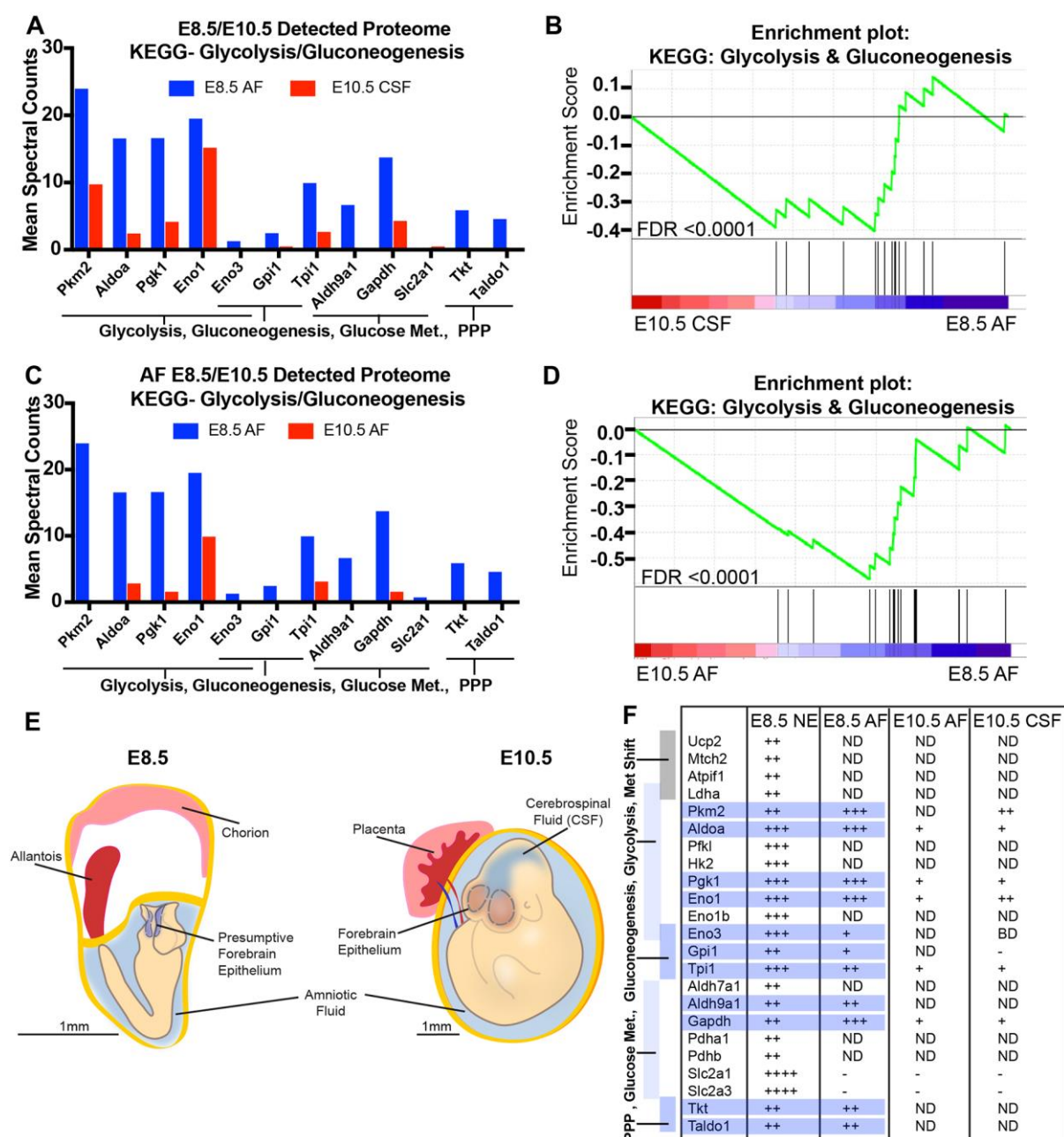


Figure 3. Downregulation of metabolic machinery in AF and CSF proteomes match concurrent transcriptional changes in forebrain. (A-B) Mass spectrometry of E8.5 AF and E10.5 CSF detected more components of glycolytic and gluconeogenic pathways in E8.5 AF than in E10.5 CSF. **(C-D)** Mass spectrometry of AF at E8.5 and E10.5 detected more components of glycolytic and gluconeogenic pathways in E8.5 AF than in E10.5 AF. **(E-F)**

The proteome of the fluid surrounding the early forebrain matched neuroepithelial gene expression patterns. +++, ≥ 15 spectral counts; ++, ≥ 10 spectral counts; +, ≥ 5 spectral counts; -, ≤ 1 spectral count; ND, not detected. (Line drawings modified from Chau et al., 2018).

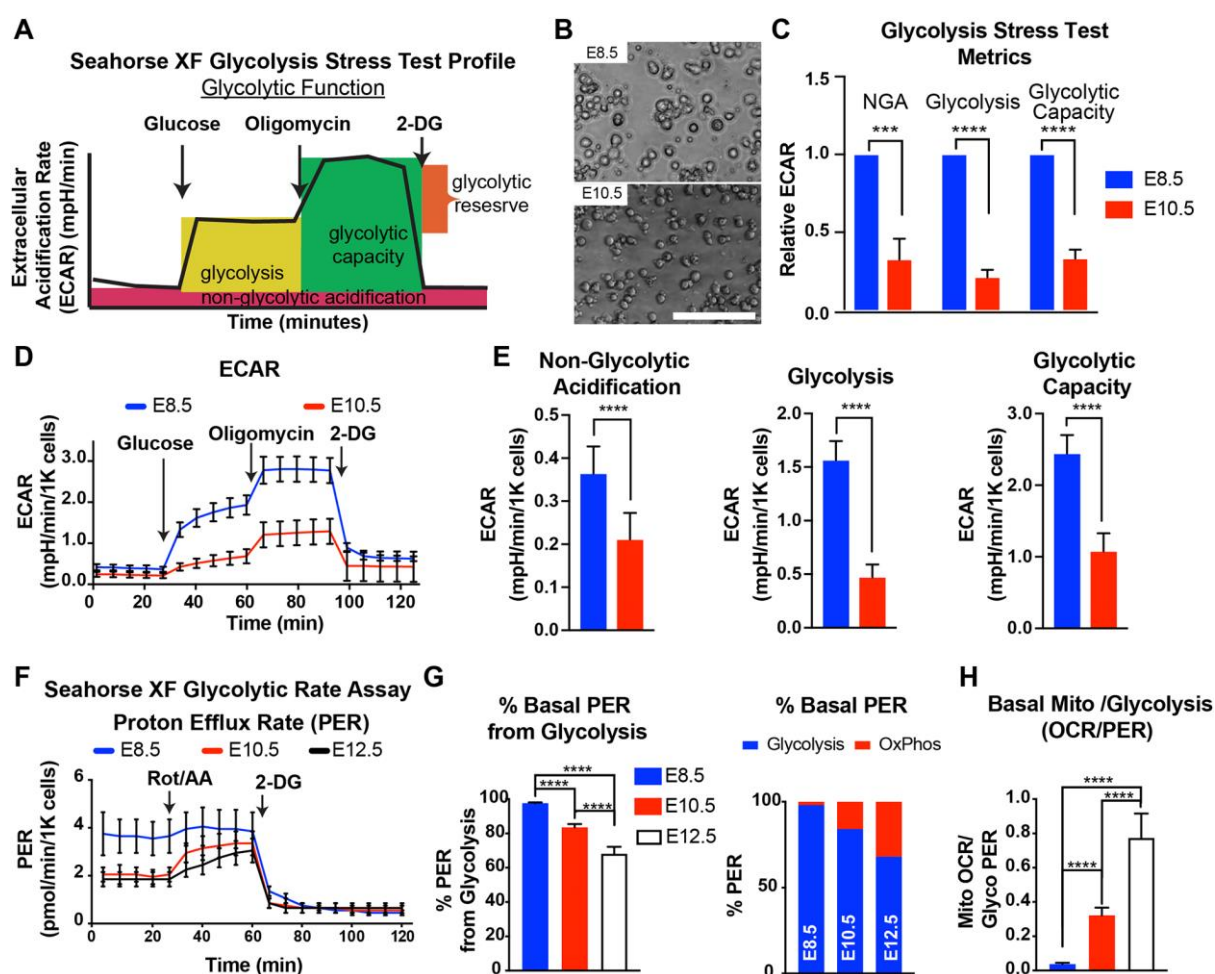


Figure 4. Glucose usage shifts in forebrain progenitors to decrease in glycolytic activity from E8.5 to E10.5 to E12.5. (A) Schematic of Agilent Seahorse XF glycolysis stress test profile measuring extracellular acidification rate (ECAR) in glucose-free media followed by sequential addition of glucose, oligomycin, and 2-deoxy-D-glucose (2-DG) used to determine glycolytic metrics in (B) primary cells from E8.5 and E10.5 neuroepithelium. (C) While non-glycolytic acidification (NGA) was higher at E8.5, acidification via glycolysis, and the overall glycolytic capacity were also higher at E8.5 vs. E10.5 (N=3 experiments), multiple t-tests: ***, $p < 0.005$; ****, $p < 0.001$, error bars = SEM. (D-E) Extracellular acidification trace and glycolytic metrics from one of the representative experiments (N=11 individuals, points

are averages of 10 wells) included in the meta-analysis in (C), multiple t-tests ***, $p < 0.005$; ****, $p < 0.001$, error bars = SEM. (F) Seahorse XF Glycolytic rate assay determines proton efflux rate (PER) under basal conditions, after inhibiting oxidative phosphorylation with rotenone/ antimycin A (Rot/AA), and after inhibiting glycolysis with 2-DG. Shown is the PER trace from the experiments included in (G-H) (N=3-9 replicate wells per age, error bars = SEM). (G) Percent of PER from glycolysis vs. oxidative phosphorylation decreased from E8.3 to E10.5 to E12.5, multiple t-tests ****, $p < 0.001$, error bars = SEM. (H) Ratio of mitochondrial oxygen consumption rate (OCR) to glycolytic PER increases as the neuroepithelium matures. Scale bar: (B) 100 μ m.

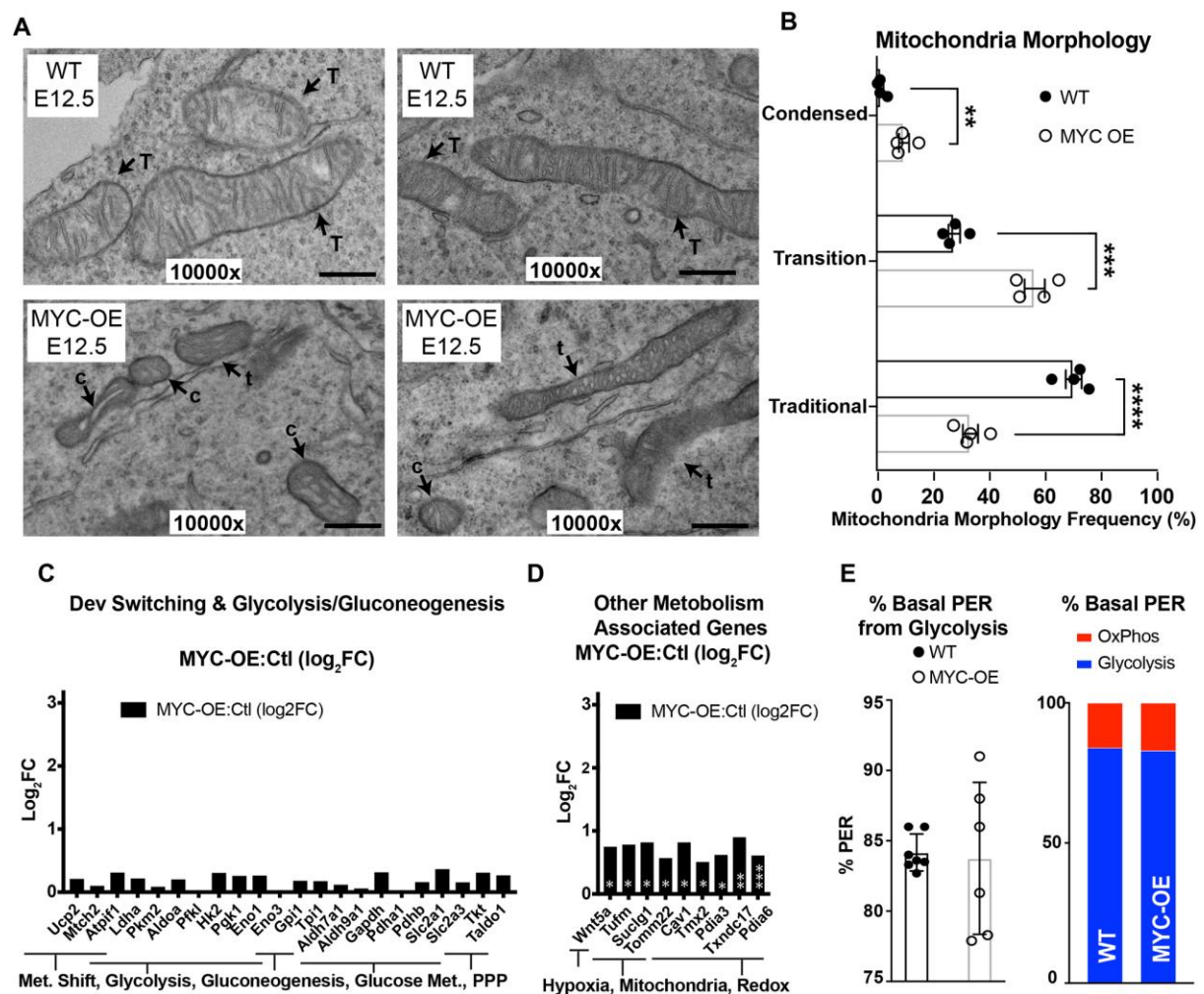


Figure 5. Mitochondrial morphology in the neuroepithelium, but not glycolysis, is dependent on developmental downregulation of MYC. (A) Mitochondrial morphology shifted to a more condensed/ immature state in E12.5 neuroepithelial cells with genetically prolonged c-MYC expression (Foxg1-cre; StopFLMYC). Arrows (black): mitochondria (annotated as T: traditional, t: transition, and c: condensed). (B) Neuroepithelial cells overexpressing c-MYC were more likely to have condensed mitochondria with dense matrix and swollen cristae, while mitochondria in control E12.5 neuroepithelial cells were more traditional with lucid matrices and thin cristae; t-test: **, $p < 0.01$; ***, $p < 0.001$; ****, $p < 0.0001$; error bars = SEM. (C) Molecular components of metabolic shifting, glycolysis,

gluconeogenesis, glucose metabolism, and PPP were unchanged after forced c-MYC expression in the E12.5 neuroepithelium (N=3 biological replicates) with respect to the control E12.5 neuroepithelium (N=3 biological replicates) (log₂fold change >0) cuffdiff v2, ns: $q > 0.1$. **(D)** Only a small number of genes associated with metabolism were affected by c-MYC overexpression in the E12.5 neuroepithelium (log₂fold change >0) cuffdiff v2 with q value: *, $q < 0.1$. **(E)** Percent of PER from glycolysis vs. oxidative phosphorylation was unchanged in neuroepithelial cells after prolonged c-MYC expression; N=3 experiments, N=7 control animals and N=6 MYC-OE animals, multiple t-tests ns, non-significant $p=0.8634$, error bars = SEM. Scale bar: (A) 500nm.

Figure S1

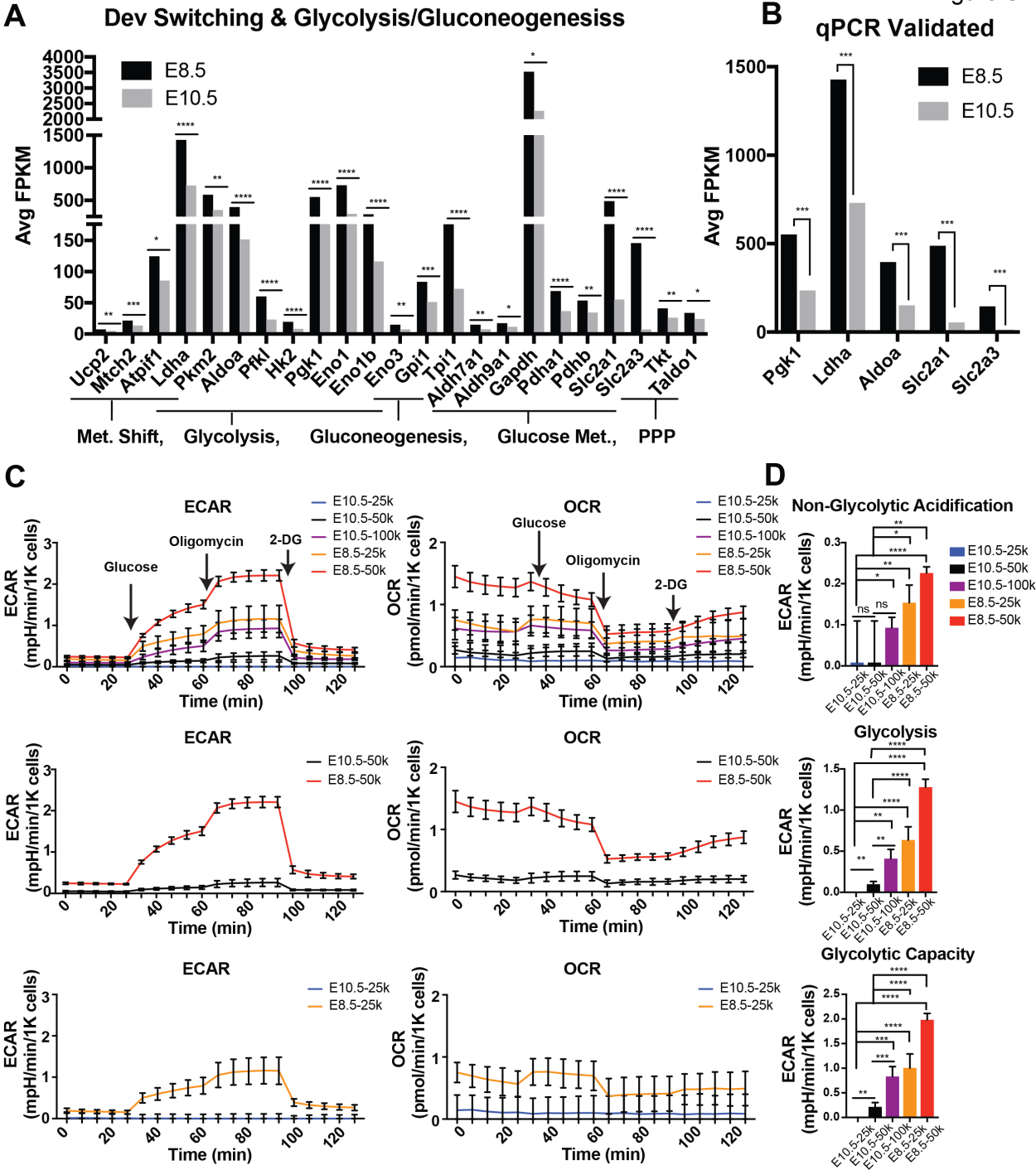


Figure S1. Gene and protein expression suggest metabolic switch away from glycolysis during E8.5 to E10.5 transition and glucose usage shifts in forebrain progenitors to decrease in glycolytic activity from E8.5 to E10.5. (A) Average FPKM values from mRNA sequencing data for genes associated with glycolysis, oxidative phosphorylation, and nucleotide biosynthesis through the pentose phosphate pathway (PPP). These pathways were enriched in the E8.5 neuroepithelium (N=2 biological replicates, each a pooled litter) with respect to the E10.5 neuroepithelium (N=2 biological replicates, each a pooled litter) (\log_2 fold change >0) cuffdiff v2 with q value: *, $q < 0.1$; **, $q < 0.001$; ***, $q < 0.0001$; ****, $q < 0.00001$; see Chau, et al 2018. (B) Average FPKM values for the individual components of these pathways (*pgk1*, *ldha*, *aldoa*, *slc2a1* (glut1), and *slc2a3* (glut3) that were validated by qPCR to be downregulated in E10.5 neuroepithelium. (C) Extracellular acidification (ECAR) and oxygen consumption rate (OCR) traces from an experiment comparing the effect of cellular density in the Seahorse Glycolysis Stress test (N=10 wells for experiments at 25k cells/ well; N=5 wells for experiments at 50k cells/ well and 100k cells, well); multiple t-tests ***, $p < 0.005$; ****, $p < 0.001$, error bars = SEM. (C) Glycolytic metrics from the different cellular density in Seahorse Glycolysis Stress test (N=10 wells for experiments at 25k cells/ well; N=5 wells for experiments at 50k cells/ well and 100k cells, well);multiple t-tests ***, $p < 0.005$; ****, $p < 0.001$, error bars = SEM. (D) This transcriptional enrichment was also reflected in protein levels. Scale bar (E) 10 μ m.

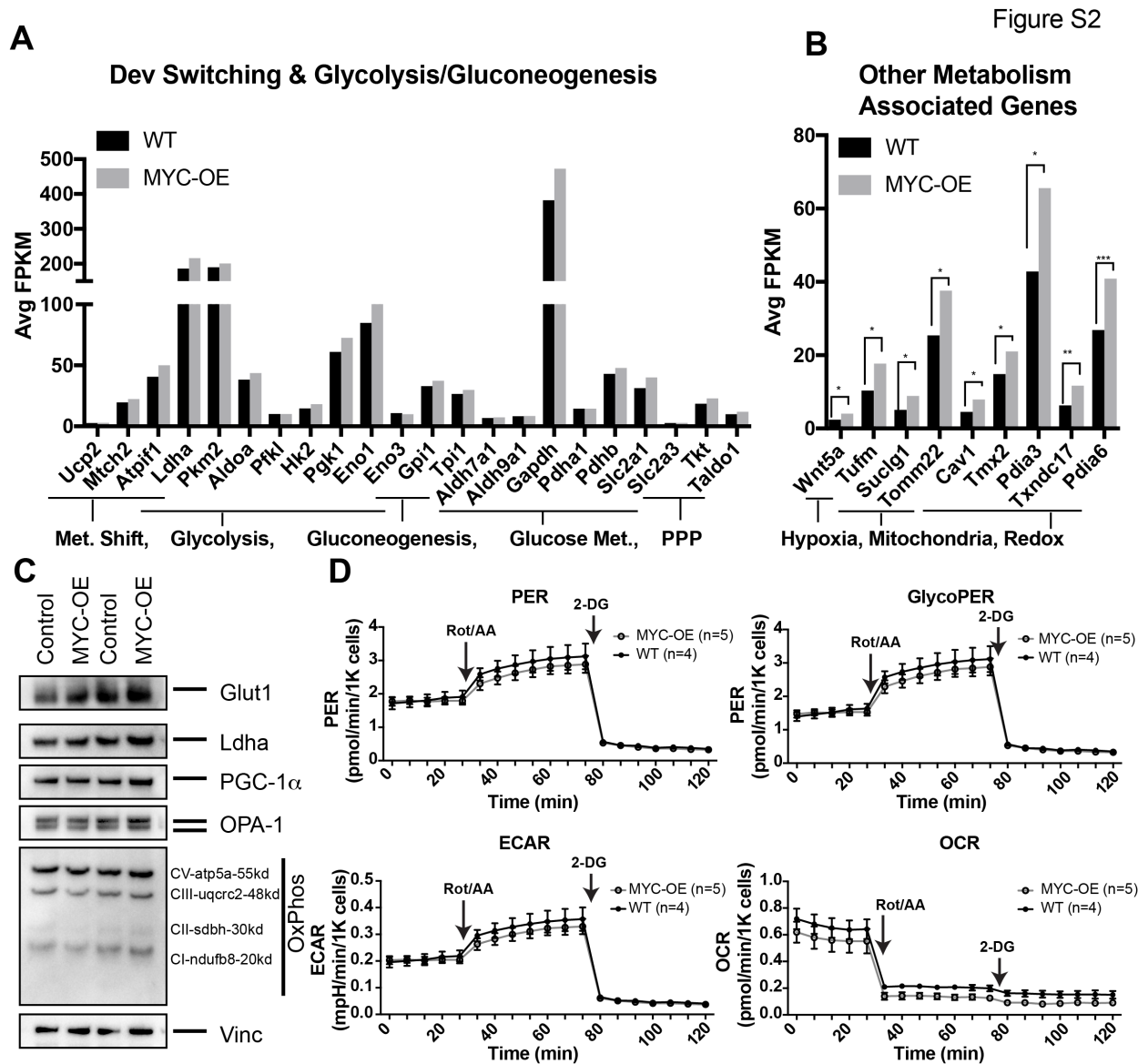


Figure S2. Mitochondrial morphology in the neuroepithelium, but not glycolysis, is dependent on developmental downregulation of MYC. (A) Average FPKM values from mRNA sequencing data for genes associated with glycolysis, oxidative phosphorylation, and nucleotide biosynthesis through the pentose phosphate pathway (PPP) were unchanged after forced c-MYC expression in the E12.5 neuroepithelium (N=3 biological replicates) with respect to the control E12.5 neuroepithelium (N=3 biological replicates) (\log_2 fold change >0) cuffdiff v2, ns: $q > 0.1$; see Chau, et al 2018. (B) Average FPKM values for genes associated with metabolism that were affected by c-MYC overexpression in the E12.5 neuroepithelium (\log_2 fold change >0) cuffdiff v2 with q value: *, $q < 0.1$. (C) Immunoblotting for canonical mitochondrial morphology component proteins PGC-1 α and OPA1, and OxPhos complex components. Vinculin was used as a loading control. (D) Traces of proton efflux rate (PER), PER from glycolysis (GlycoPER); extracellular acidification rate (ECAR), and oxygen consumption rate (OCR) for the Seahorse Glycolytic Rate Assay in neuroepithelial cells after prolonged c-MYC expression; N=2 experiments, N=4 control animals and N=5 MYC-OE animals, error bars = SEM.